minerals

MDPI

Article

A Novel Surface Passivation Method of Pyrite within Rocks in Underwater Environments to Mitigate Acid Mine Drainage at Its Source

Lijun Fan, Tiancheng Han, Xianxing Huang, Yixuan Yang, Tao Zhu, Weiwei Zhai, Daoyong Zhang and Xiangliang Pan *

Key Laboratory of Microbial Technology for Industrial Pollution Control of Zhejiang Province, College of Environment, Zhejiang University of Technology, Hangzhou 310014, China; fanlijun@zjut.edu.cn (L.F.); 211122270026@zjut.edu.cn (T.H.); xxhuang759039@163.com (X.H.); 15053763483@163.com (Y.Y.); 2112127085@zjut.edu.cn (T.Z.); weiweizhai@zjut.edu.cn (W.Z.); zhangdaoyong@zjut.edu.cn (D.Z.)
* Correspondence: panxl@zjut.edu.cn

Abstract: Mitigating acid mine drainage (AMD) at its source, specifically within rocks containing pyrite in underwater environments, poses a significant environmental challenge worldwide. Existing passivation techniques are primarily designed for open-air conditions, involving direct contact with coating materials at a solid–liquid interface, making them ineffective beneath a water barrier. In this study, we introduce a novel passivation method inspired by the design of underwater bio-adhesives. Tannic acid (TA) combined with polyethylene glycol (PEG) was employed to form a hydrophobic film directly on the pyrite surface, overcoming water resistance and addressing the limitations of current techniques. Electrochemical experiments and chemical leaching experiments were conducted to evaluate the oxidation resistance of the passivating films. TA–PEG-coated pyrite exhibited a lower oxidation rate and a higher static contact angle of 126.2°, achieving suppression efficiencies of 71.6% for total Fe release and 68.1% for total S release. A comprehensive characterization approach, including scanning electron microscopy (SEM), Fourier transform infrared spectroscopy (FTIR), Raman spectroscopy, and X-ray photoelectron spectroscopy (XPS), was employed to investigate the passivation mechanism. The results of this study may provide new insights into the preparation of simpler and greener passivating agents to suppress pyrite oxidation at its source in underwater environments.

Keywords: acid mine drainage; pyrite; TA–PEG coating; passivation; water-filled mining tunnels; source control

Citation: Fan, L.; Han, T.; Huang, X.; Yang, Y.; Zhu, T.; Zhai, W.; Zhang, D.; Pan, X. A Novel Surface Passivation Method of Pyrite within Rocks in Underwater Environments to Mitigate Acid Mine Drainage at Its Source. *Minerals* **2024**, *14*, 973. https://doi.org/10.3390/min14100973

Academic Editor: Giovanni Grieco

Received: 27 August 2024
Revised: 23 September 2024
Accepted: 26 September 2024
Published: 27 September 2024

1. Introduction

Acid mine drainage (AMD) is a significant environmental issue faced by the mining industries, driven by the continuing worldwide mining exploitation, metal extraction, and coal cleaning [1,2]. AMD occurs when sulfide minerals (mainly pyrite, FeS_2) in mining rocks, mine wastes, and associated tailings storage facilities are exposed to oxidizing conditions, e.g., water and oxygen [3–7]. AMD may stem from the oxidative leaching of sulfides in open waste piles; in addition, a considerable portion is from pit lakes and water-filled mining tunnels [8–10]. The prolonged discharge of AMD, along with its severe environmental threat and the associated substantial remediation costs, establishes it as a globally challenging environmental issue. Consequently, it is imperative to develop strategies to inhibit AMD formation.

Until now, predominant methods for AMD treatments encompass both end-of-pipe treatments and source control. Source control, aiming to prevent its formation from the origin [11], is a more promising technique for AMD treatment compared to end-of-pipe treatments. It included sterilization [12], cover isolation [13,14], and surface passivation [10]. Among these methods, surface passivation is highly desirable for AMD source treatment

by forming a protective layer on the pyrite surface or specifically binding to reactive surface sites to restrict O_2, H_2O, and bacteria access. It can be classified into four types: (1) inorganic coatings [15]; (2) organic coatings [10,16]; (3) carrier-microencapsulation (CME) [8,17–19]; and (4) organosilane coatings [20–25]. These conventional passivating agents have demonstrated the capability to reduce the oxidation rate of pyrite. However, these passivation methods face challenges in water-filled mining environments, especially for vertical shafts or pit lakes, where AMD is a prevalent issue. Current passivation techniques for pyrite have primarily been developed for waste piles in relatively open-air conditions. However, the solid–liquid interface between water and the pyrite surface underwater can render the passivation process ineffective beneath the water barrier.

The challenges presented by underwater environments lie in overcoming the obstacles imposed by water barriers [26,27]. Water flows can pose a challenge as they may induce the dilution of passivation agents, consequently reducing their effectiveness. Furthermore, the adherence of passivators to surfaces beneath the water barrier is a complex task, and the water can hinder intermolecular interactions between the passivator and pyrite surface. These limitations may impede the practical implementation of passivation in the water-filled mining environment. Hence, there is an imperative for a facile and green strategy to form passivating layers on the pyrite surface to suppress AMD production within rocks in the water-filled mining environment.

Tannic acid (TA), a polyphenolic molecule, has a well-established history of application as an antioxidant, bio-sorbent, and adhesive, owing to its intrinsic properties [28,29]. It is widely distributed in nature and can be extracted from various parts of plants [28–30]. Recently, TA has gained increased attention in the design and development of wet adhesive materials due to its strong molecular glue properties and eco-friendliness [27]. TA contains several catechol groups in its molecular structure, which can act as chelating agents for metal ions, such as Fe(II), Fe(III), Cu(II), and Zn(II), enabling the deposition of TA–metal complexes films on various substrates [29,31,32]. These chelating abilities facilitate the preparation of hydrophobic TA–metal complexes films with low solubilities and good antioxidant properties [28,33].

Moreover, the dihydroxyphenyl and trihydroxyphenyl groups in TA serve as hydrogen bond donors, forming strong hydrogen bonds with molecules containing hydrogen bond acceptors [27,34]. Recently, various bio-adhesives with appealing wet adhesive properties have been synthesized through the physical crosslinking of polymers and TA via numerous hydrogen bonds [35]. Notably, Lee et al. demonstrated that a mixture of polyethylene glycol (PEG) and TA can produce a water-based yet water-resistant bio-adhesive through a hydrogen bond donor [27]. PEG, known for its low toxicity, has been used in a variety of adhesives and binders in daily life and industrial fields [36]. Chen et al. synthesized a TA-based PEG adhesive through a simple polycondensation reaction under mild conditions (0–25 °C), exhibiting favorable antibacterial and antioxidative properties [34]. In a recent study, Li and colleagues developed a scale-like hydrophobic coating on pyrite surfaces by crosslinking TA with PropS-SH, effectively reducing pyrite oxidation rates [37].

In light of these findings, we propose the formation of a self-crosslinking passivating layer comprising TA and PEG on pyrite surfaces with the aid of Fe ions. This TA–PEG passivator can be easily prepared using accessible materials and simple procedures, enabling in situ passivation of pyrite surfaces in water-filled mining environments. Furthermore, this passivator may exhibit the rapid self-healing, pH-stimuli responsive, and free radical scavenging abilities attributed to the intrinsic character of TA [28,30,38], rendering it highly advantageous in water-filled mining environments.

This study aims to assess the feasibility of employing TA and PEG to form passivating layers on pyrite surfaces beneath water, addressing the limitations of existing techniques. The suppression efficiency of pyrite oxidation and the forming mechanism of passivating layers are evaluated by electrochemical measurements, chemical leaching experiments, and other structure or morphology characterization techniques. The surface hydrophobia is analyzed by water contact angle measurement. This work may offer a potential solution

for mitigating pyrite oxidation at its source within water-filled mining environments, addressing a challenging and prevalent issue worldwide.

2. Materials and Methods

2.1. Materials

The pyrite (FeS_2) used in this study was sourced from the Shangbao Mineral market, Hunan Province, China. To make the working electrodes for electrochemical measurements, the pyrite was first cut into 10 mm × 10 mm × 10 mm cubes. The remaining pyrite samples were then crushed, ground, and sieved to less than 200 mesh (75 μm). Power X-ray diffraction (XRD) analysis indicated that the sample was mainly composed of pyrite and quartz with minor impurities (Figure S1). X-ray fluorescence (XRF) analysis showed that the pyrite contained 55.95 wt. % Fe and 30.85 wt. % S, with trace impurities of 2.18 wt. % As, 3.62 wt. % O, 0.07 wt. % Al, and 0.05 wt. % Pb.

The tannic acid (TA, $C_{76}H_{52}O_{46}$, 95%) and polyethylene glycol (PEG, $HO(CH_2CH_2O)_nH$, 95%) used in this study were purchased from Aladdin Co., Ltd. (Shanghai, China). All chemicals were used without further purification throughout the experiments. Before the experiments, the mineral cubes were polished using 1200 # carbide paper to obtain fresh surfaces. The pyrite powder was prewashed with a 1 M HCl solution, followed by rinsing with deionized (DI) water and 95% acetone, and finally freeze-dried for later experiments.

2.2. Passivating Process

To evaluate the passivation performance of TA and TA–PEG on the pyrite surface in water-filled mining environments, 1 g of pyrite powder was weighed into 250 mL wide-mouth high-density polyethylene (HDPE) bottles containing 50 mL of DI water for 24 h to stimulate real underwater conditions. Subsequently, 50 mL of the prepared stock coating solutions of TA with and without the PEG addition were added into the bottles to obtain a final TA concentration of 5 g/L and PEG concentrations of 0, 0.1, 1.0, 2.0, and 5.0 g/L, respectively. The selected TA concentration of 5 mg/L was in accordance with previous studies [37,39]. All the bottles were stirred magnetically and then stabilized for 6 h at room temperature. The supernatant was then discarded, and the residue was dried at room temperature for 24 h to evaluate its passivating ability later. The pyrite electrode coating process was performed similarly to the pyrite powder coating method. The resulting passivated pyrites were labeled as follows: TA-, TA-0.1–PEG-, TA-1.0–PEG-, TA-2.0–PEG-, and TA-5.0–PEG-coated pyrite, respectively. Pyrites coated with different concentrations of PEG in the presence of TA were collectively referred to as TA–PEG-coated pyrite. The untreated pyrite was designated as uncoated pyrite.

2.3. Electrochemical Measurements

To assess the passivating abilities of the coatings obtained, electrochemical measurements were performed, including electrochemical impedance spectroscopy (EIS), Tafel polarization curve (Tafel), and cyclic voltammetry curve (CV) measurements, as described in previous studies [40]. The Reference 600 electrochemical workstation (CH660, CH Instruments, China) was used for electrochemical measurements with a conventional three-electrode cell. The uncoated or coated pyrite electrode, Pt foil electrode (10 mm × 10 mm), and saturated calomel electrode (SCE) served as working, counter, and reference electrodes, respectively. The working electrode was assembled following the method described by Li et al. [23,24,37,39]. Specifically, the pyrite cubes (before or after coating) were connected to copper wires using conducting silver glue and sealed with epoxy resin, leaving the passivated surface exposed to the electrolyte. A 0.2 M Na_2SO_4 solution with a pH of 2.0 (adjusted with H_2SO_4) was used as the electrolyte. Before the electrochemical measurements, open circuit potential (OCP) tests were conducted to ensure the stability of the system. The polarization curves were obtained by sweeping the electrode potential automatically from −650 to +650 mV (vs. OCP) at a scan rate of 2.0 mV/s. The EIS measurements were performed with a frequency range of 0.001–10,000 Hz and a peak-to-peak amplitude of

10 mV. The impedance data were fitted with ZSimpWin 3.20 (2004) software. Triplicate measurements were conducted to ensure the reproducibility of the results.

2.4. Chemical Leaching Experiments

To evaluate the passivation performances of different passivated pyrite samples, pH, total Fe, and total S release were measured in the leachates. A short-time leaching experiment was conducted by adding 100 mL of HCl solution (pH = 1.0) into the HDPE bottles containing the uncoated and a series of coated pyrites for 48 h. The bottles were then sealed using a lid with a 5 mm hole to ensure full atmospheric contact and minimal evaporation. The chosen pH value and the leaching experiments conducted at room temperature under quiescent conditions without agitation were to stimulate natural AMD environments. The leachate pH values were checked daily and stability was maintained by adding a few drops of 1 M NaOH or 1 M HCl solution as needed. Five mL subsamples were taken at 0, 1, 4, 8, 12, 24, 36, and 48 h and passed through 0.22 μm filters for subsequent analysis. The extracted subsamples were compensated by adding 5 mL of HCl solution to stabilize the leachate volume. In addition, the group with the best passivation effect was selected for a long-term (three-stage, each stage lasting 7 days) chemical leaching experiment to evaluate the persistence of passivating layers on the pyrite surface, compared to uncoated pyrite, under renewable leaching solutions. Here, the TA-5.0 PEG group was chosen for the test. The leaching procedures for each stage were the same as those described above, except that 100 mL of fresh HCl solution was replaced every 7 days for three stages, denoted as stages I, II, and III. The total Fe and total S release in the leachates were measured using inductively coupled plasma-optical emission spectroscopy (ICP-OES; iCAP7000, Thermo Fisher Scientific, Waltham, MA, USA). Here, the concentration of total Fe includes the dissolved ferrous (Fe(II)) and ferric (Fe(III)) ions. All leaching experiments were performed in triplicate to ensure the repeatability of the results.

2.5. Characterization

XRD analysis of the fresh sample powder was performed using an X' pert PRO X-ray diffractometer instrument (PANAlytical, Almelo, The Netherlands) with Cu Kα radiation (λ = 1.541 Å) generated at 40 kV and 40 mA. The XRD pattern was recorded over a 2θ range of 10 to 80°, with a step-size of 0.05° and an acquisition time of 2 s. The XRD pattern of the pristine sample exhibited characteristic peaks primarily corresponding to pyrite (JCPDS #42-1340), with lower intensity peaks of quartz (JCPDS # 46-1045). The bulk elemental compositions of the pyrite powder were determined by XRF using a ZSX Primus II instrument (Rigaku, Tokyo, Japan) equipped with a rhodium anode.

The surface morphologies of the uncoated and coated pyrites were observed using scanning electron microscopy (SEM; Gemini 500, Zeiss, Oberkochen, Germany). Changes in solid phases were determined by X-ray photoelectron spectroscopy (XPS; AXIS Ultra DLD, Shantz-KRATOS, Japan) equipped with an Al-Kα source at 30 eV and a step-size of 0.05 eV. XPS survey, C 1s, S 2p, Fe 2p, and O 1s high-resolution spectra were recorded as per ref. [37,41]. All high-resolution XPS spectra were aligned using the C 1s peak for adventitious carbon (284.8 eV). The data were deconvoluted using XPSPeak4.1 software, and a Shirley-type background was subtracted before being fitted by an asymmetric Gaussian–Lorentzian sum function. Fourier transform infrared spectroscopy (FTIR) was performed to analyze the functional groups using a Nicolet iS50 Fourier transform infrared spectrometer (Thermo Fisher Scientific, Waltham, MA, USA) in the range of 4000–500 cm^{-1} with a resolution of 4 cm^{-1}, and 32 scans were averaged per sample. Raman spectra were measured by using a Horiba Jobin Yvon R-HR spectrometer (LabRAM HR Evolution, Horiba, Villeneuve d'Ascq, France) with 785 nm laser excitation. The spectra were acquired with a resolution of 4 cm^{-1} in the spectral range of 2000–200 cm^{-1}, and the laser power was set to 20 mW. The hydrophilic and hydrophobic properties of the passivating film were determined by measuring the water contact angle using a contact angle analyzer (JNO, TP-50, Beijing, China).

3. Results and Discussion

3.1. Electrochemistry Results

The oxidation of pyrite results in the release of Fe ions, sulfate, and an increase in environmental acidity [36]. The oxidation rate of pyrite is a crucial parameter to evaluate the effectiveness of the passivating layer on its surface. EIS and Tafel polarization measurements were used to provide information on the electrolytic process and the passivation abilities of different passivation treatments (TA, TA-0.1 PEG, TA-1.0 PEG, TA-2.0 PEG, TA-5.0 PEG) on pyrite surfaces. EIS can provide valuable insights into the antioxidation abilities of the passivating films, as it reveals critical aspects of electrochemical kinetics, as well as the resistances and capacitances involved in electrochemical reactions [42].

The Nyquist plots of the EIS data for different pyrite electrodes are displayed in Figure 1a. Normally, Nyquist plots consist of two capacitive loops. The high-frequency capacitive loop is associated with the passive film resistance R_f, attributed to impedance coupling and pseudo-capacitance, while the low-frequency loop is the charge transfer resistance R_{ct}, representing the resistance between the electrode and outer Helmholtz layer [42]. As shown in Figure 2a, uncoated and coated pyrite electrodes exhibit a single capacitive reactance arc, and the semicircle diameters of the capacitance arc increased with the addition of TA and PEG. Based on this analysis, Figure 1b depicts the corresponding equivalent circuit model ($R_s(Q_1(R_{ct}(Q_2R_f)))$), which effectively simulates the uncoated/coated pyrite/electrolyte interface. The obtained impedance parameters are summarized in Table 1. Here, R_s donates the ohmic resistance of the electrolyte, R_{ct} represents the charge transfer of pyrite oxidation, and R_f represents the resistance of the surface passive film. The constants Q_1 and Q_2 represent the electric capacities of the double-layers at the electrode/electrolyte interface and the passivating film at the pyrite surface, respectively.

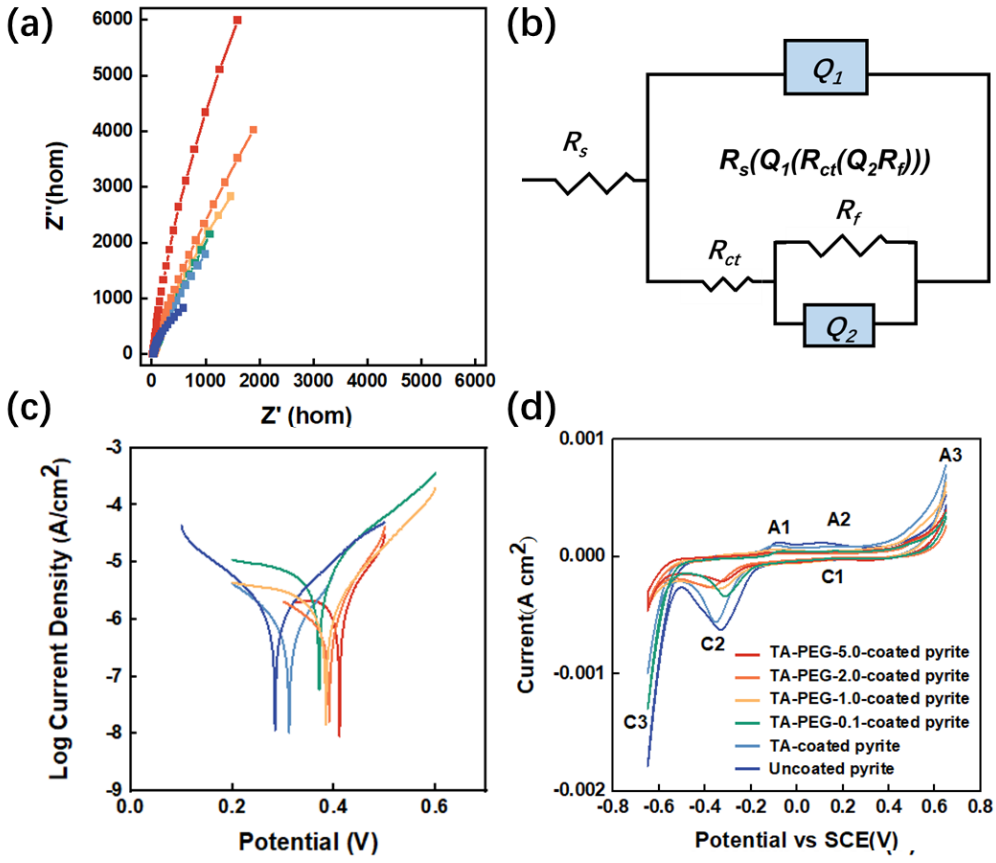

Figure 1. (**a**) Nyquist plots; (**b**) equivalent electrical circuit model; (**c**) Tafel polarization curves; (**d**) CV curves. All measurements were conducted in a 0.2 M Na_2SO_4 electrolyte with a pH value of 2.0.

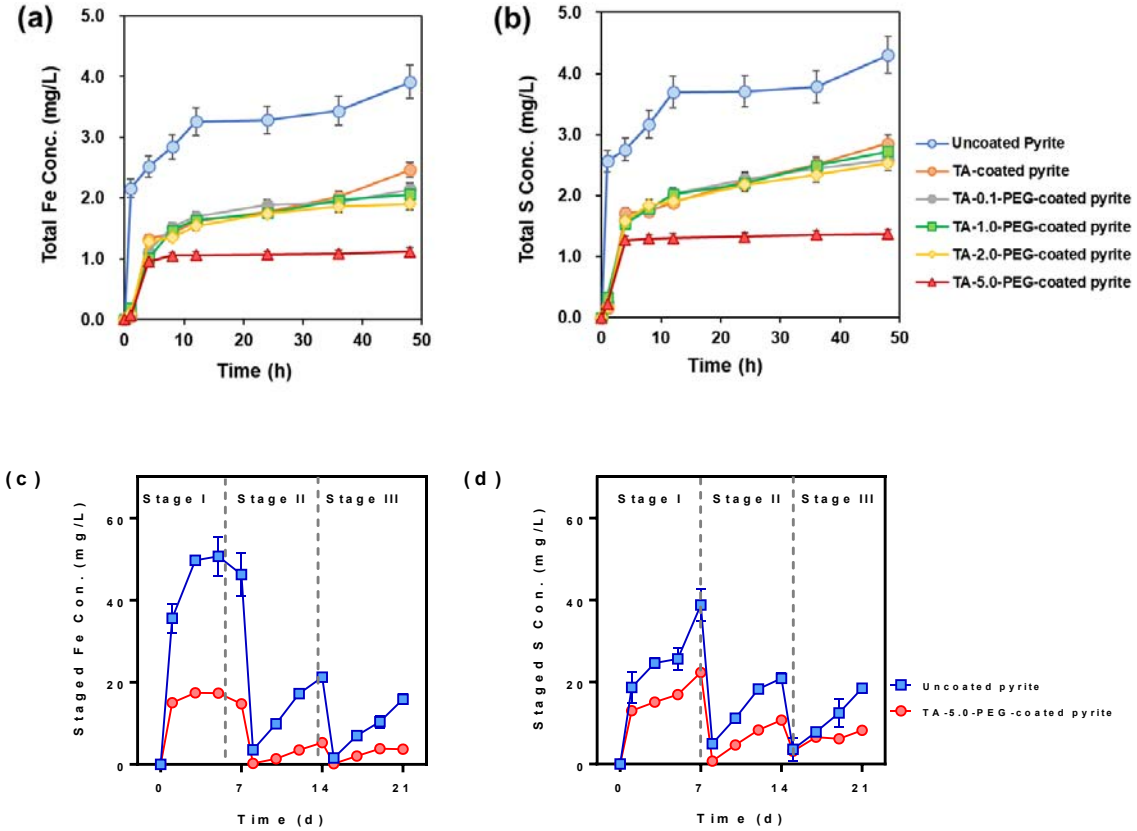

Figure 2. Effects of different passivation on the antioxidation ability of pyrite: evolution of total Fe (**a**) and total S (**b**) concentrations in leachates of uncoated and a series of coated pyrites over 48 h. Staged Fe (**c**) and total S (**d**) concentrations in uncoated pyrite and TA-5.0–PEG-coated pyrite (hereafter referred to as stages I, II, and III, with a duration of 7 days per stage); 100 mL of HCl solution (pH = 1.0) was refreshed between stages. Standard deviations (n = 3) were represented by error bars.

Table 1. Fitting parameters of the equivalent circuit diagram for uncoated and coated pyrite electrodes.

Electrodes	R_s/Ω·cm^2	Q_1		R_{ct}/10^4 Ω·cm^2	Q_2		R_f/10^4 Ω·cm^2
		Y_1/10^{-4} S/s^n cm^{-2} n			Y_2/10^{-4} S/s^n cm^{-2} n		
Uncoated pyrite	30.9	4.1	0.9	1.8	37.9	0.8	0.8
TA-coated pyrite	35.7	3.6	0.8	3.6	32.5	0.8	1.9
TA-0.1–PEG-coated pyrite	38.3	3.1	0.8	5.9	25.4	0.8	2.8
TA-1.0–PEG-coated pyrite	38.9	3.1	0.9	10.7	17.8	0.6	19.8
TA-2.0–PEG-coated pyrite	39.2	2.9	0.9	11.2	19.7	0.9	27.1
TA-5.0–PEG-coated pyrite	34.1	1.7	0.9	15.6	16.4	0.6	39.7

According to the electrochemical parameters of different pyrite electrodes, it can be observed that the addition of TA and higher concentrations of PEG exhibited higher R_{ct} and R_f values. These results reveal larger capacitive reactance arc diameters of TA–PEG-coated pyrite electrodes compared to uncoated and pure-TA-coated pyrite electrodes. Among all the electrodes, the TA-5.0–PEG-coated pyrite electrode exhibited the highest R_{ct} and R_f values, which were 8.6 and 49.7 times higher than those of the uncoated pyrite electrode, and 2.0 and 2.4 times greater than those of the pure TA-coated pyrite electrode. The larger values of the parameter R_{ct} and R_f, or the bigger semicircle diameters of the capacitance arc in Nyquist plots, suggest a stronger antioxidant capacity of the passivating film on the pyrite surface and a lower surface oxidation rate [42]. The pyrite electrode coated with 5.0 g/L TA and 5.0 g/L PEG showed the slowest electron transfer rate and the best passivation performance among all the tested pyrite electrodes, indicating that TA and PEG

can act synergistically to form a denser passivating film on the pyrite surface, resulting in a significantly enhanced antioxidation ability, particularly at a PEG dosage of 5 g/L.

Tafel polarization curves were used to obtain different passivated pyrite oxidation rates and further used to evaluate the electrochemical behavior of uncoated and passivated pyrite electrodes. The corrosion potential (E_{corr}) and the corrosion density (i_{corr}) are critical parameters in assessing the corrosion behavior of the passivating film. A more positive E_{corr} indicates better corrosion resistance or higher stability, while a larger i_{corr} reflects a faster corrosion rate of the passivating film. As shown in Figure 1c, similar Tafel polarization curves for the different passivation agents suggest a comparable pyrite oxidation mechanism. Furthermore, with the addition of TA and higher PEG, the polarization curve presented obvious rightward shifts, which indicated an increase in corrosion potential values (E_{corr}). The corresponding electrochemical corrosion parameters of our investigated electrodes fitted by the Tafel extrapolation method are presented in Table 2.

Table 2. Tafel polarization kinetic parameters of uncoated and coated pyrite electrodes.

Electrodes	E_{corr} (mV/SCE)	i_{corr} (μA/cm^2)
Uncoated pyrite	284	6.71
TA-coated pyrite	312	4.09
TA-0.1–PEG-coated pyrite	371	3.12
TA-1.0–PEG-coated pyrite	384	2.51
TA-2.0–PEG-coated pyrite	389	2.35
TA-5.0–PEG-coated pyrite	411	1.89

The experimental results here indicate that the addition of TA and higher concentrations of PEG results in lower corrosion density (i_{corr}), which inhibits pyrite oxidation by increasing pyrite polarization resistance. Specifically, the i_{corr} values of uncoated pyrite, TA-coated pyrite, and TA-5.0–PEG-coated pyrite electrodes decreased successively, with values of 6.71, 4.09, and 1.89 μA/cm^2, respectively. These results indicate that the addition of TA and PEG inhibits pyrite oxidation, resulting in inhibiting efficiencies (η) of 39.0% (TA-coated pyrite) and 71.8% (TA-5.0–PEG-coated pyrite), where η is defined as $\eta\% = (i_{corr} - i_{0corr})/i_{0corr} \times 100$ according to previous studies [43]. Here, i_{corr} and i_{0corr} are the corrosion current densities of the uncoated pyrite and TA or TA-5.0–PEG-coated pyrite, respectively. Meanwhile, the corrosion current potentials (E_{corr}) of different pyrite electrodes are inversely proportional to the change in the i_{corr} values, which are 284 mV (uncoated pyrite), 312 mV (TA-coated pyrite), and 411 mV (TA-5.0–PEG-coated pyrite), respectively. Generally, a larger E_{corr} and a smaller i_{corr} indicated stronger oxidation resistance of the pyrite electrode. Our experimental results showed that TA-5.0–PEG-coated pyrite electrodes had the optimum anti-corrosion ability, which is consistent with the experimental EIS results. This paragraph describes Figure 1c, but only specific values (those shown in Table 2) are discussed.

CV curves were employed to provide information about the redox reactions on various pyrite electrodes and to study the specific oxidation processes of pyrite with different passivating films. As depicted in Figure 1d, it was clear that all curves exhibited similar voltammograms at different passivation conditions, indicating identical electrochemical interaction mechanisms. Figure 1d shows three anodic (donated as A1, A2, and A3) and three cathodic (donated as C1, C2, and C3) peaks on the curves. During the positive scan, the first anode peak (A1) at about 0.0 V, the second (A2) at 0.2 V, and the third (A3) at 0.7 V represent the oxidation reactions of S(-II) in pyrite to elemental sulfur, Fe(II) in pyrite to produce Fe(III), and the produced elemental sulfur to form SO_4^{2-}, respectively. Correspondingly, in the reverse scan, the first cathodic peak (C1) appeared at 0.2 V, the second (C2) at −0.3 V, and the third (C3) at −0.7 V, all of which may be associated with the reduction reactions of Fe(III) hydroxide to Fe(II), FeS_2 to FeS or H_2S, and H^+ to H_2, respectively, based on previous reports [37]. It was evident that the uncoated pyrite electrode had the highest oxidation and reduction peak current intensities. However, the incorporation of TA and PEG

significantly reduced the current intensities, indicating improved antioxidant properties of the passivating film. Furthermore, the TA-5.0–PEG-coated pyrite electrode exhibited the lowest current signal, indicating minimal electrochemical reactions on its surface and the best antioxidant ability. The CV curves demonstrated that the combination of TA and PEG had a good passivation effect on the pyrite surface, especially for the TA-5.0–PEG-coated pyrite, which is consistent with the EIS and Tafel polarization measurements.

3.2. Chemical Leaching Experiments

The series of electrochemical measurements confirmed that TA–PEG-coated pyrite has a significantly improved antioxidative ability compared to uncoated pyrite and TA-coated pyrite, especially for the TA-5.0–PEG-coated pyrite. To clarify this phenomenon, chemical leaching experiments were conducted using HCl with a pH of 1.0 to simulate the dissolution process of pyrite under extremely acidic conditions.

The evolution of total Fe and S concentrations in the leachates with different passivators over 48 h and three stages are illustrated in Figure 2a,b respectively. In Figure 2a, the concentrations of Fe and S increased rapidly in the first four hours, after which the release rate decelerated to varying degrees and stabilized at certain values for the remaining hours. The final concentrations of total Fe and S from uncoated pyrite were 4.0 and 4.4 mg/L after 48 h, respectively, which were significantly higher than those of the coated pyrite. The values for TA-5.0–PEG-coated pyrite were 1.1 g/L of total Fe and 1.4 g/L of total S, respectively. The oxidation rates of pyrite coated with TA and TA-5.0–PEG decreased by 33.7% and 71.6% (based on total Fe concentrations) and 48.1% and 68.1% (based on S concentrations), respectively. Compared to uncoated pyrite, the pyrite coated with TA and PEG exhibited a significant enhancement in oxidation resistance, which is in accordance with the electrochemical measurements. Based on the results of the 48 h leaching experiments, it can be concluded that the TA–PEG passivator demonstrated effective inhibition of pyrite oxidation, and the optimal passivation performance was achieved at a PEG dosage of 5.0 mg/L. These findings are consistent with the electrochemical measurements.

To further investigate the stability of the TA–PEG passivation layer, we conducted a three-stage (7 days per stage) chemical leaching experiment to compare total Fe and S concentrations in the leachate of uncoated and TA-5.0–PEG-coated pyrite, with leachate refreshment between stages. As shown in Figure 2b, the patterns of total Fe and S concentrations in the leachate of uncoated pyrite and TA-5.0–PEG-coated pyrite were similar throughout the experiment, but the magnitudes were different. Here, the concentrations of Fe and S released in stages II and III did not include the Fe and S released in the previous stages, which cannot represent the total released Fe and S concentration. The concentrations of released Fe and S in TA-5.0–PEG-coated pyrite were significantly lower than those in uncoated pyrite. During stage I, the final Fe release for uncoated pyrite reached 46.2 mg/L, whereas, for TA-5.0–PEG-coated pyrite, the rate and extent of pyrite oxidation were significantly suppressed, resulting in a reduced final Fe release of only 14.6 mg/L. The corresponding final S releases were 38.8 mg/L and 22.3 mg/L, respectively. The subsequent stage reaffirmed this suppression effect. The Fe and S concentrations in stages II and III were still significantly lower compared to stage I. In stage II, Fe concentrations in the leachates reached ∼21.3 mg/L for the uncoated pyrite and ∼5.3 mg/L for the TA-5.0–PEG-coated pyrite groups. At the same time, S concentrations rose to 20.9 mg/L and 10.7 mg/L, respectively. In stage III, the Fe and S releases were consistently lowest in both passivation groups. Specifically, Fe release for uncoated pyrite was 15.9 mg/L, while for coated pyrite, it reduced to 3.7 mg/L. Similarly, the corresponding S releases were 18.5 mg/L for uncoated pyrite and 8.2 mg/L for coated pyrite. Compared to uncoated pyrite, the oxidation rate of pyrite coated with TA-5.0–PEG decreased by 55.3% (based on Fe concentrations in all three stages) and 41.1% (based on S concentrations in all three stages), respectively. Overall, the TA–PEG-coated pyrite demonstrated the best oxidation resistance and good stability, which is consistent with the results obtained from the electrochemical measurements.

3.3. Characterization of the Coated Pyrite

3.3.1. Surface Morphology of Coatings Using SEM

To observe the morphological changes of pyrite surface before and after passivation, the SEM method was utilized to characterize the uncoated pyrite, TA-, and TA–PEG-coated pyrite samples, as shown in Figure 3. The surface of uncoated pyrite (Figure 3a) was relatively smooth, and only a small number of mineral particles caused during the grinding process were attached to the uncoated pyrite surface. A thicker, adhesive, scale-like coating was formed on the surface of TA-5.0–PEG-coated pyrite (Figure 3f). Compared with uncoated pyrite, both the TA- and TA–PEG-coated pyrite exhibited relatively thicker layers at the pyrite surface with more mineral particles attached, and the surface became coarser with increasing PEG concentrations.

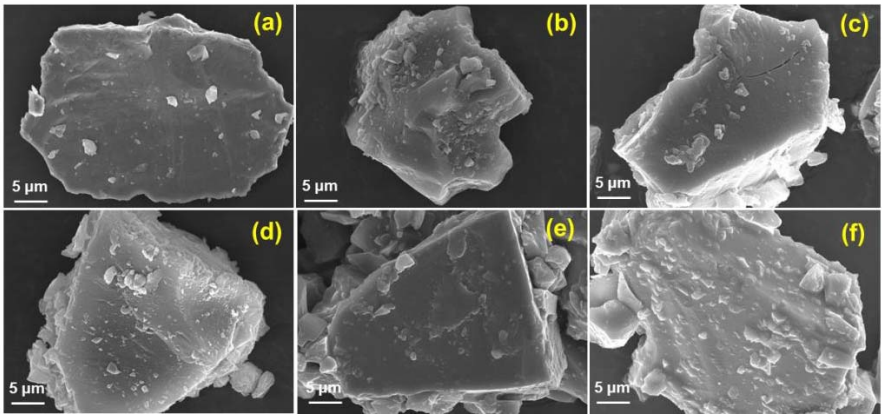

Figure 3. SEM images of (**a**) uncoated pyrite; (**b**) TA-coated pyrite; (**c**) TA-0.1–PEG-coated pyrite; (**d**) TA-1.0–PEG-coated pyrite; (**e**) TA-2.0–PEG-coated pyrite; and (**f**) TA-5.0–PEG-coated pyrite.

After a 21-day chemical leaching experiment, the surface layers on uncoated and TA-5.0–PEG-coated pyrite showed distinct morphological differences (Figure S2). The passivating layer formed on the surface of TA–PEG-coated pyrite was much smoother and flatter, with fewer scattered fragments, compared to uncoated pyrite. The surface of uncoated pyrite became much rougher and was covered with more scattered fragments after the three-stage leaching experiment. However, the TA–PEG passivating film remained flat and smooth with few changes. These clear differences in passivating layers on the pyrite surface demonstrated that the combination of TA and PEG passivators can effectively passivate the pyrite surface and provide good antioxidant capacity.

3.3.2. Wettability Properties of Coatings

Water molecules are one of the primary oxidizing media during the process of pyrite oxidation, and they play a critical role in accelerating this process. Therefore, the hydrophobicity of the passivating layer is a vital factor in suppressing pyrite oxidation by resisting water corrosion to a certain extent.

To assess changes in surface wettability, water contact angle measurements were conducted on both uncoated and coated pyrites, as presented in Figure 4. The results showed that the surface layer of uncoated pyrite exhibited poor hydrophobicity, with a water contact angle of only 81.5° (Figure 4a), mainly due to the presence of iron sulfides and iron hydroxides on its surface. The water contact angle of TA-coated pyrite (Figure 4b) increased to 102.8°, attributed to the complexation between TA and Fe(II)/(III), which was higher than the result (46.8°) reported by Li et al. (2023) [37], which might be attributed to relatively higher values of the selected pyrite samples. The prewashing process could dissolve the surface iron hydroxides, increasing the hydrophobicity of the pyrite surface. Furthermore, the measured contact angle of the series of TA–PEG-coated pyrite increased significantly to 109.6°, 111.4°, 116.7°, and 126.2° when coated with 0.1 g/L, 1.0 g/L, 2.0 g/L, and 5.0 g/L of PEG, respectively. The increase in water contact angle indicates an improve-

ment in the hydrophobicity of the passivating film, which is crucial in resisting water corrosion and suppressing pyrite oxidation. These results highlighted that the TA–PEG passivating layer has superior corrosion resistance against water in natural environments, which reduces the possibility of pyrite surface oxidation. The SEM characterization is consistent with the contact angle results, as a dense and crosslinked coating is formed through the synergistic reaction of TA and PEG at the pyrite surface, effectively increasing the hydrophobicity of the pyrite surface. Therefore, both SEM and static water contact angle measurements demonstrated that the TA and PEG passivating layer has a better corrosion-resistant microstructure.

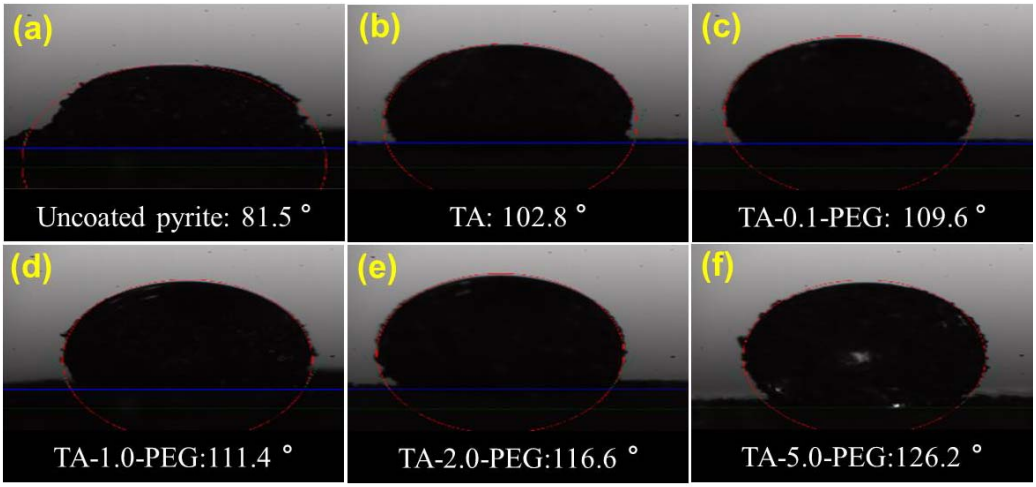

Figure 4. (**a**–**f**) Static water contact angles of uncoated and coated pyrites.

3.4. Mechanism of Passivation Coatings

3.4.1. FTIR Analysis

To analyze the interactions between pyrite and TA and PEG, FTIR spectra of uncoated pyrite were compared with those of TA-coated pyrite and TA-5.0–PEG-coated pyrite, which showed the best passivation ability, as shown in Figure 5a. The dominant IR frequencies recorded in pristine pyrite were 1047, 771, and 690 cm^{-1}. The broad peak at approximately 1047 cm^{-1} was attributed to S-S stretching vibrations in the pyrite lattice [44]. Additionally, the peaks at 771 cm^{-1} and 690 cm^{-1} were due to the symmetric stretching of Si–O and the bending mode of Si–O–Si, respectively, resulting from the presence of quartz in pyrite samples [45,46].

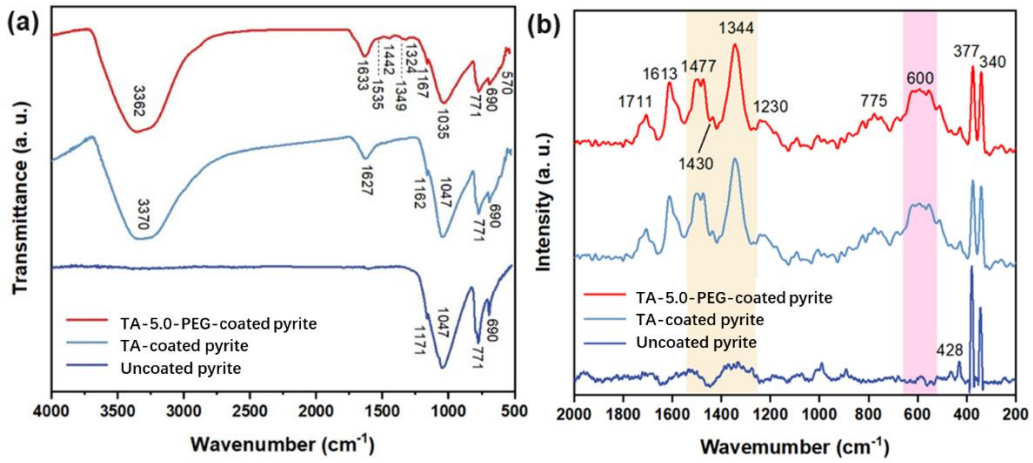

Figure 5. FTIR (**a**) and Raman spectra (**b**) of uncoated pyrite, TA-coated pyrite, and TA-5.0–PEG-coated pyrite.

The FTIR analysis revealed that in addition to the characteristic pyrite bands, the TA and TA-5.0–PEG composite passivating layers displayed additional peaks at 1627–1633 and 3362–3370 cm^{-1}, corresponding to ester and hydroxyl groups of TA, respectively [35]. The peaks associated with the –OH stretching vibrations of free catechol/pyrogallol molecules in TA (3370 cm^{-1}) were observed to shift to the lower wavenumber at 3362 cm^{-1} in TA–PEG-coated pyrite, and the peaks related to the carbonyl band (C=O) in TA-coated pyrite shifted to the higher wavenumber (1627 to 1633 cm^{-1}) in TA–PEG-coated pyrite. These shifts likely resulted from the formation of H–bonds, leading to a change in the vibrational energy of the –OH and C=O bonds, which was consistent with previous studies [35]. The FTIR results suggested intermolecular interactions between PEG and TA via hydrogen during the co-assembly process.

In the case of TA–PEG-coated pyrite, new characteristic peaks appeared at 1442 and 1324 cm^{-1}, resulting from the symmetrical stretching of the deprotonated carboxylic acid groups in TA and the deprotonation and chelation of TA and Fe ions in pyrite (Fe–O–C bonds) [47]. This indicated that the hydroxyl and carboxyl groups in TA can chelate with Fe ions to form a passivating layer on the pyrite surface. Additionally, a new band observed at 570 cm^{-1} was assigned to the Fe–O band of the TA–Fe complex [31,48].

In summary, the appearance of new peaks in the FTIR spectra provided evidence to explain the formation of passivating layers on the pyrite surface. Initially, TA absorbs on the pyrite surface through the chelation of its hydroxyl groups with Fe ions, forming Fe–O–C bonds. Subsequently, hydrogen bonding occurs between PEG and TA molecules, as indicated by a shift in –OH and C=O bonds. This process promotes the formation of an enhanced self-assembly network that effectively covers the pyrite surface.

3.4.2. Raman Analysis

The Raman spectroscopy results provided further evidence for the interactions between pyrite, TA, and PEG. As shown in Figure 5b, the Raman spectra in the region 2000–200 cm^{-1} were recorded. The peaks appearing at 428, 377, and 340 cm^{-1} were observed in all samples and were attributed to pyrite [49]. In TA- and TA–PEG-coated pyrite, the bands in 1711, 1613, and 1477 cm^{-1} were associated with the ester group in pure TA [36]. Moreover, the peaks at 600, 1344, and 1477 cm^{-1}, associated with the chelation of Fe(II)/Fe(III) by the phenolic oxygen of TA, were observed, which were absent in the uncoated pyrite spectra [36]. These observations provide compelling evidence of the successful coating of the complexes on the pyrite surface.

3.4.3. XPS Analysis

The successful incorporation of the passivating film was confirmed by XPS analysis, as shown in Figures 6, S3 and S4. The characteristic peaks of Fe 2p, O 1s, C 1s, and S 2p were detected in the binding energy range of 0–1350 eV (Figure S3). There were some differences in the signal intensities of different elements among the different coated pyrites. The characteristic signals of C 1s in TA- and TA–PEG-coated pyrites were stronger due to the cooperation of TA and PEG. The Fe 2p and S 2p peaks in uncoated pyrite, TA-coated pyrite, and TA–PEG-coated pyrite weakened successively, indicating that the surface of pyrite had been successfully coated by TA and PEG [35–37,40,41].

After fitting the high-resolution XPS spectra of different elements, the changes in chemical bonds on the surfaces of uncoated, TA-coated, and TA-5.0–PEG-coated pyrite were further analyzed. The relative curve fitting parameters of the XPS deconvolution and references for each peak assignment are summarized in Table S1. The deconvolution of the C 1s spectra is illustrated in Figure 6a. The C 1s spectrum of the uncoated pyrite can be decomposed into three different components: C=O/O-C=O, C-O, and C-C species located at 288.75 eV, 286.50 eV, and 284.80 eV, respectively, which might be due to the adsorption of adventitious carbonaceous material on the pyrite surface [41,50,51]. The corresponding spectra for TA- and TA–PEG-coated pyrites both showed a new peak at

283.5 eV that was assigned to C=C [52], indicating that TA-containing C=C successfully covered the pyrite surface.

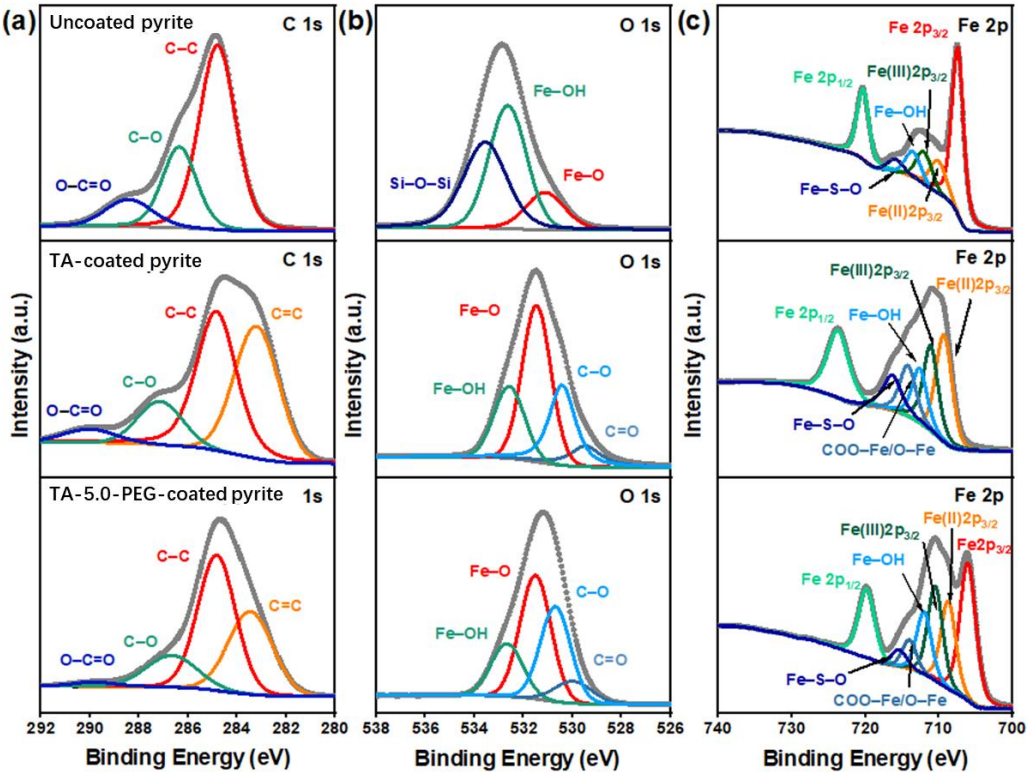

Figure 6. XPS spectra of C 1s (**a**), O 1s (**b**), and Fe 2p (**c**) of uncoated pyrite, TA-coated pyrite, and TA-5.0–PEG-coated pyrite.

The O 1s deconvolution spectra are illustrated in Figure 6b. For the uncoated pyrite, three peaks were observed at 531.10, 532.65, and 533.60 eV, corresponding to Fe-O, Fe-OH, and Si-O, respectively [39]. Conversely, new peaks appeared in TA- and TA–PEG-coated pyrites at 530.40 and 529.45 eV, which were assigned to C-O and C=O, respectively [53]. The relative peak areas showed that the peak representing Fe-O in TA-coated pyrite was higher than that of uncoated pyrite, indicating the successful adsorption and chelation of TA onto the pyrite surface. In comparison to TA-coated pyrite, the intensities of the peak of Fe-O, and C=O decreased, while that of C-O increased, further confirming the adsorption of PEG onto the TA molecules.

The Fe 2p XPS spectra were used to characterize the oxidation states of the pyrite surfaces. The deconvolution of the Fe 2p peak is shown in Figure 6c. In the uncoated pyrite, the signals at 707.40, 710.20, 712.20, and 720.40 eV were characteristic of Fe 2p $_{3/2}$, Fe(II) 2p $_{3/2}$, Fe(III) 2p $_{1/2}$, and Fe 2p $_{1/2}$, respectively [54]. Meanwhile, the peaks located at 713.65 eV and 715.95 eV were the characteristic signals of Fe-OH and Fe-S-O, respectively [39]. No Fe satellite peaks were observed, as Fe(II) in pyrite is in a low-spin configuration. These results suggest surface oxidation of pyrite, leading to the production of iron sulfates and iron oxides. However, the major component in the sample remained pyrite. In TA- and TA–PEG-coated pyrites, similar peaks were observed but weakened, and a new peak at 714.10 was detected, attributable to COO-Fe/Fe-O [54]. This confirms that TA has successfully cheated with Fe ions, generating TA–Fe complexes that passivated the pyrite surface.

In addition to Fe 2p XPS, S 2p XPS was also utilized to characterize the oxidation states of pyrite surfaces. As shown in Figure S4, the peaks observed at 170.65/169.45 eV, 165.4/164.25 eV, and 163.85/162.65 eV were assigned to 2p $_{1/2}$ and 2p $_{3/2}$ of sulfate, polysulfide, and pyrite, respectively [54–56]. The peak intensity of the oxidation product sulfate was

much greater for uncoated pyrite compared to TA- and PEG-coated pyrite, indicating a lower degree of surface oxidation for the coated samples.

3.4.4. Summary of Passivating Mechanism on the Pyrite Surface

Based on the results obtained and discussed above, we propose a formation mechanism for the TA–PEG passivating layers on the pyrite surface beneath the water environment, as illustrated in Figure 7. Initially, TA molecules can adhere to pyrite and provide polydentate ligands that coordinate with metal ions, leading to the formation of metal-polyphenol complexes. Specifically, TA molecules were found to coordinate with Fe(II) on the pyrite surface, as well as Fe(III) produced by the partial oxidation of pyrite, complexes of TA–Fe(II) and TA–Fe(III) can be formed. The deposition of these complexes leads to the formation of a protective passivating film on the pyrite surface, hindering the dissolution of the pyrite. Subsequently, TA molecules can self-assemble with polymer (PEG) chains through multidentate hydrogen bonds with the aid of Fe ions or other metal ions, crosslinking these polymer chains into a network. This process further strengthens the passivating layers, effectively suppressing pyrite oxidation in aquatic conditions.

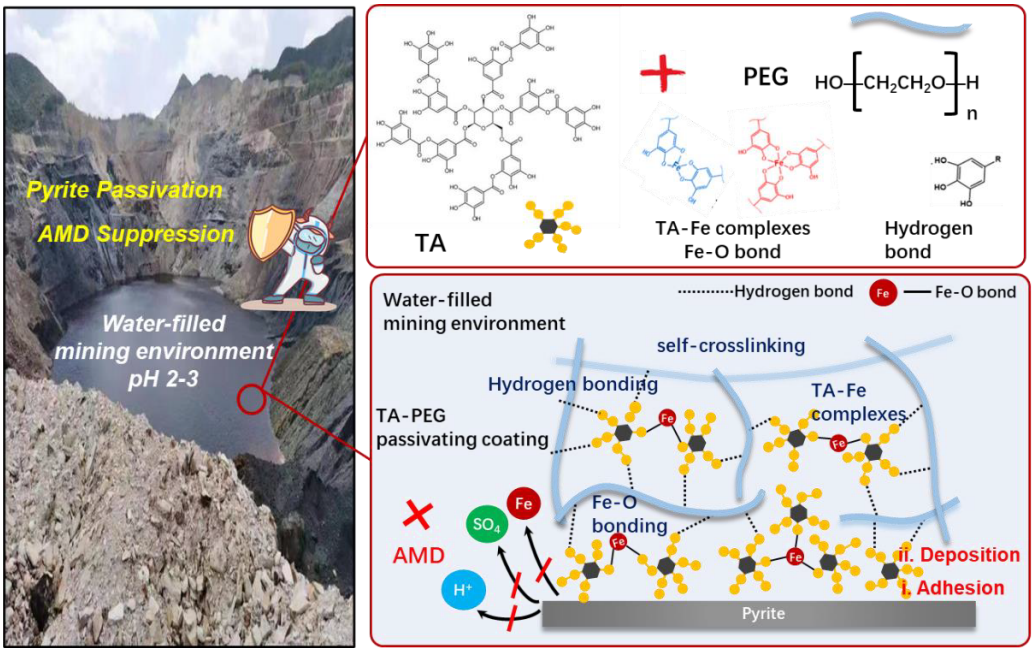

Figure 7. Illustration of the formation mechanism of the TA–PEG passivating coating on the pyrite surface in water-filled mining environments.

4. Conclusions

In summary, we report a simple and greener method to passivate the pyrite surface by crosslinking two commercially available materials, PEG and TA, offering a potential solution for mitigating pyrite oxidation at its source within water-filled mining environments, a challenging and prevalent issue worldwide. Our electrochemistry tests and chemical leaching experiments demonstrated that the TA-5.0–PEG passivator had superior antioxidation ability compared to uncoated and pure-TA-coated pyrite. Additionally, SEM and static water contact angle measurements revealed that the TA–PEG passivating layer formed on the pyrite surface was dense and compact, leading to a significant enhancement of its surface hydrophobicity. Furthermore, FTIR, Raman, and XPS were used to elucidate the mechanism of passivating layer formation on the pyrite surface.

Notably, the TA–PEG passivator can be easily prepared by simply mixing two commercially available materials, PEG and TA, without the need for a complicated and high-temperature coating process. This is a significant advantage for practical applications. Moreover, the passivation process does not require specialized equipment. TA molecules

can efficiently bond with Fe and other metal ions (e.g., Cu, Zn, Al) in AMD by utilizing their polydentate ligands. Additionally, TA can crosslink with PEG chains to form a strong and compact TA–PEG passivation coating on the pyrite surface. The incorporation of a crosslinking agent (TA) could reduce the degree of swelling of PEG to keep the effectiveness of the passivating layer. The in situ combination of TA and PEG has been demonstrated to effectively passivate the pyrite surface beneath the water to suppress the production of AMD at its source. It is important to note, however, that the current study utilized pure pyrite immersed in simplified acidic leachate to evaluate the passivation efficacy of the TA–PEG composite passivation treatment. In the natural environment, pure pyrite rarely exists in isolation; instead, pyrite typically occurs as grains of various sizes embedded within silicate rocks, often coated with iron oxyhydroxides or existing in diverse geochemical forms. This heterogeneity can significantly influence the TA–PEG passivation effect. Although our study has provided clear evidence of the TA–PEG composite's effectiveness in suppressing pyrite oxidation and reducing AMD production under controlled laboratory conditions, its applicability in complex natural systems requires further investigation. The real-world suppression of AMD is influenced by numerous variables, such as the composition of surrounding rocks, the presence of other minerals, and the fluctuating environmental conditions.

Therefore, future studies should focus on optimizing the TA–PEG passivation treatment to better align with the diverse geochemical realities encountered in AMD-affected environments. Additionally, the impact of this treatment on the immobilization of associated metal ions, such as Zn, Cu, and As, which are often mobilized during AMD formation, must be systematically evaluated to ensure both the effectiveness and environmental safety of the passivation method. Expanding research in this area will be critical for developing a robust and practical solution for AMD suppression in the field.

Supplementary Materials: The following supporting information can be downloaded at https://www.mdpi.com/article/10.3390/min14100973/s1, Figure S1: The XRD spectrum of the pyrite sample; Figure S2: SEM images of uncoated pyrite (a,c) and TA-5.0–PEG-coated pyrite (b,d) before and after a 21-day chemical leaching experiment; Figure S3: XPS full spectra of uncoated, TA-, and TA-5.0–PEG-coated pyrite; Figure S4: XPS devolution spectra of S 2p of uncoated, TA-, and TA-5.0–PEG-coated pyrite; Table S1: XPS fitting of C 1s, O 1s, Fe 2p, and S 2p of uncoated pyrite, TA, and TA-5.0–PEG-coated pyrite.

Author Contributions: Conceptualization, L.F. and X.P.; methodology, L.F.; software, T.H.; validation, T.H., X.H. and T.Z.; formal analysis, L.F.; investigation, Y.Y.; resources, L.F.; data curation, W.Z.; writing—original draft preparation, L.F.; writing—review and editing, W.Z. and D.Z.; visualization, L.F.; supervision, X.P.; project administration, L.F.; funding acquisition, L.F. All authors have read and agreed to the published version of the manuscript.

Funding: This work was funded by the National Natural Science Foundation of China (42107215).

Data Availability Statement: The authors confirm that the data supporting the findings of this study are available within the article and supplementary materials.

Conflicts of Interest: The authors declare that they have no known competing financial interests or personal relationships that could have appeared to influence the work reported in this paper.

References

1. Hudson-Edwards, K. Tackling mine wastes. *Science* **2016**, *352*, 288–290. [CrossRef] [PubMed]
2. Nordstrom, D.K. Mine waters: Acidic to circmneutral. *Elements* **2011**, *7*, 393–398. [CrossRef]
3. Fan, L.; Zhao, F.; Liu, J.; Hudson-Edwards, K.A. Dissolution of realgar by *Acidithiobacillus ferrooxidans* in the presence and absence of zerovalent iron: Implications for remediation of iron-deficient realgar tailings. *Chemosphere* **2018**, *209*, 381–391. [CrossRef] [PubMed]
4. Burton, E.D.; Karimian, N.; Hamilton, J.L.; Frierdich, A.J. Iron Isotopes in Acid Mine Drainage: Extreme and Divergent Fractionation between Solid (Schwertmannite, Jarosite, and Ferric Arsenate) and Aqueous Species. *Environ. Sci. Technol.* **2022**, *56*, 18060–18068. [CrossRef] [PubMed]

5. Hammond, C.M.; Root, R.A.; Maier, R.M.; Chorover, J. Arsenic and iron speciation and mobilization during phytostabilization of pyritic mine tailings. *Geochim. Cosmochim. Acta* **2020**, *286*, 306–323. [CrossRef]
6. Von Gunten, K.; Bishop, B.; Plata Enriquez, I.; Alam, M.S.; Blanchard, P.; Robbins, L.J.; Feng, R.; Konhauser, K.O.; Alessi, D.S. Colloidal transport mechanisms and sequestration of U, Ni, and As in meromictic mine pit lakes. *Geochim. Cosmochim. Acta* **2019**, *265*, 292–312. [CrossRef]
7. Fan, L.; Zhu, T.; Yang, Y.; Han, T.; Qiao, Z.; Huang, X.; Zhai, W.; Pan, X.; Zhang, D. Iron colloidal transport mechanisms and sequestration of As, Ni, and Cu along AMD-induced environmental gradients. *Sci. Total. Environ.* **2023**, *898*, 165513. [CrossRef] [PubMed]
8. Park, I.; Tabelin, C.B.; Jeon, S.; Li, X.; Seno, K.; Ito, M.; Hiroyoshi, N. A review of recent strategies for acid mine drainage prevention and mine tailings recycling. *Chemosphere* **2019**, *219*, 588–606. [CrossRef]
9. Ren, Y.; Cao, X.; Wu, P.; Li, L. Experimental insights into the formation of secondary minerals in acid mine drainage-polluted karst rivers and their effects on element migration. *Sci. Total. Environ.* **2023**, *858*, 160076. [CrossRef] [PubMed]
10. Tu, Z.; Wu, Q.; He, H.; Zhou, S.; Liu, J.; He, H.; Liu, C.; Dang, Z.; Reinfelder, J.R. Reduction of acid mine drainage by passivation of pyrite surfaces: A review. *Sci. Total. Environ.* **2022**, *832*, 155116. [CrossRef]
11. Anekwe, I.M.S.; Isa, Y.M. Bioremediation of acid mine drainage—Review. *Alexandria Eng. J.* **2023**, *65*, 1047–1075. [CrossRef]
12. Qian, G.; Schumann, R.C.; Li, J.; Short, M.D.; Fan, R.; Li, Y.; Kawashima, N.; Zhou, Y.; Smart, R.S.C.; Gerson, A.R. Strategies for Reduced Acid and Metalliferous Drainage by Pyrite Surface Passivation. *Minerals* **2017**, *7*, 42. [CrossRef]
13. Pabst, T.; Bussiere, B.; Aubertin, M.; Molson, J. Comparative performance of cover systems to prevent acid mine drainage from pre-oxidized tailings: A numerical hydro-geochemical assessment. *J. Contam. Hydrol.* **2018**, *214*, 39–53. [CrossRef]
14. Beauchemin, S.; Clemente, J.S.; Thibault, Y.; Langley, S.; Gregorich, E.G.; Tisch, B. Geochemical stability of acid-generating pyrrhotite tailings 4 to 5 years after addition of oxygen-consuming organic covers. *Sci. Total. Environ.* **2018**, *645*, 1643–1655. [CrossRef] [PubMed]
15. Pierre Louis, A.M.; Yu, H.; Shumlas, S.L.; Van Aken, B.; Schoonen, M.A.; Strongin, D.R. Effect of Phospholipid on Pyrite Oxidation and Microbial Communities under Simulated Acid Mine Drainage (AMD) Conditions. *Environ. Sci. Technol.* **2015**, *49*, 7701–7708. [CrossRef]
16. Acharya, B.S.; Kharel, G. Acid mine drainage from coal mining in the United States—An overview. *J. Hydrol.* **2020**, *588*, 125061. [CrossRef]
17. Park, I.; Higuchi, K.; Tabelin, C.B.; Jeon, S.; Ito, M.; Hiroyoshi, N. Suppression of arsenopyrite oxidation by microencapsulation using ferric-catecholate complexes and phosphate. *Chemosphere* **2021**, *269*, 129413. [CrossRef]
18. Li, X.; Park, I.; Tabelin, C.B.; Naruwa, K.; Goda, T.; Harada, C.; Jeon, S.; Ito, M.; Hiroyoshi, N. Enhanced pyrite passivation by carrier-microencapsulation using Fe-catechol and Ti-catechol complexes. *J. Hazard. Mater.* **2021**, *416*, 126089. [CrossRef]
19. Park, I.; Tabelin, C.B.; Seno, K.; Jeon, S.; Ito, M.; Hiroyoshi, N. Simultaneous suppression of acid mine drainage formation and arsenic release by Carrier-microencapsulation using aluminum-catecholate complexes. *Chemosphere* **2018**, *205*, 414–425. [CrossRef]
20. Yu, M.; Feng, J.; Yang, Q.; Dang, Z.; Zhang, L. Inhibition of organosilane/ATP@HQ self-healing passivator for pyrite oxidation. *Chemosphere* **2022**, *287*, 132342. [CrossRef]
21. Ouyang, Y.; Liu, Y.; Zhu, R.; Ge, F.; Xu, T.; Luo, Z.; Liang, L. Pyrite oxidation inhibition by organosilane coatings for acid mine drainage control. *Miner. Eng.* **2015**, *72*, 57–64. [CrossRef]
22. Dong, Y.; Zeng, W.; Lin, H.; He, Y. Preparation of a novel water-soluble organosilane coating and its performance for inhibition of pyrite oxidation to control acid mine drainage at the source. *Appl. Surf. Sci.* **2020**, *531*, 147328. [CrossRef]
23. Li, D.; Gong, B.; Liu, Y.; Dang, Z. Self-healing coatings based on PropS-SH and pH-responsive HNT-BTA nanoparticles for inhibition of pyrite oxidation to control acid mine drainage. *Chem. Eng. J.* **2021**, *415*, 128993. [CrossRef]
24. Liu, Y.; Hu, X.; Xu, Y. PropS-SH/SiO_2 nanocomposite coatings for pyrite oxidation inhibition to control acid mine drainage at the source. *J. Hazard. Mater.* **2017**, *338*, 313–322. [CrossRef] [PubMed]
25. Feng, J.; Zhou, C.; Yang, Q.; Dang, Z.; Zhang, L. Performance and mechanisms of PropS-SH/Ce(dbp)(3) coatings in the inhibition of pyrite oxidationtion for acid mine drainage control. *Environ. Pollut.* **2023**, *322*, 121162. [CrossRef] [PubMed]
26. Messersmith, R.E.; Bartlett, M.E.; Rose, D.J.; Smith, D.A.; Patchan, M.W.; Benkoski, J.J.; Trexler, M.M.; Hoffman, C.M. Rapid Underwater Adhesive Utilizing Crosslinker and Amine Catalyst-Filled Microcapsules. *ACS Appl. Polym. Mater.* **2021**, *3*, 996–1002. [CrossRef]
27. Lee, D.; Hwang, H.; Kim, J.S.; Park, J.; Youn, D.; Kim, D.; Hahn, J.; Seo, M.; Lee, H. VATA: A Poly(vinyl alcohol)- and Tannic Acid-Based Nontoxic Underwater Adhesive. *ACS Appl. Mater. Interfaces* **2020**, *12*, 20933–20941. [CrossRef]
28. Guo, Z.; Xie, W.; Lu, J.; Guo, X.; Zhao, L. Tannic Acid-based Metal Phenolic Networks for Bio-applications: A Review. *J. Mater. Chem. B* **2021**, *9*, 4098–4110. [CrossRef]
29. Pucci, C.; Martinelli, C.; De Pasquale, D.; Battaglini, M.; di Leo, N.; Degl'Innocenti, A.; Belenli Gumus, M.; Drago, F.; Ciofani, G. Tannic Acid-Iron Complex-Based Nanoparticles as a Novel Tool against Oxidative Stress. *ACS Appl. Mater. Interfaces* **2022**, *14*, 15927–15941. [CrossRef] [PubMed]
30. Gülçin, İ.; Huyut, Z.; Elmastaş, M.; Aboul-Enein, H.Y. Radical scavenging and antioxidant activity of tannic acid. *Arabian J. Chem.* **2010**, *3*, 43–53. [CrossRef]
31. Kaghazchi, L.; Naderi, R.; Ramezanzadeh, B. Construction of a high-performance anti-corrosion film based on the green tannic acid molecules and zinc cations on steel: Electrochemical/Surface investigations. *Constr. Build. Mater.* **2020**, *262*, 120861. [CrossRef]

32. Magdalena, K. Chelation of Cu(II), Zn(II), and Fe(II) by tannin constituents of selected edible nuts. *Int. J. Mol. Sci.* **2009**, *10*, 5485–5497. [CrossRef] [PubMed]
33. Ejima, H.; Richardson, J.J.; Liang, K.; Best, J.P.; Koeverden, M.P.V.; Such, G.K.; Cui, J.; Caruso, F. One-Step Assembly of Coordination Complexes for Versatile Film and Particle Engineering. *Science* **2013**, *341*, 154–157. [CrossRef] [PubMed]
34. Chen, C.; Geng, X.W.; Pan, Y.H.; Ma, Y.N.; Ma, Y.X.; Gao, S.Z.; Huang, X.J. Synthesis and characterization of tannic acid-PEG hydrogel via Mitsunobu polymerization. *RSC Adv.* **2020**, *10*, 1724–1732. [CrossRef] [PubMed]
35. Wang, Z.; Zhang, S.; Zhao, S.; Kang, H.; Wang, Z.; Xia, C.; Yu, Y.; Li, J. Facile biomimetic self-coacervation of tannic acid and polycation: Tough and wide pH range of underwater adhesives. *Chem. Eng. J.* **2021**, *404*, 127069. [CrossRef]
36. Espina, A.; Canamares, M.V.; Jurasekova, Z.; Sanchez-Cortes, S. Analysis of Iron Complexes of Tannic Acid and Other Related Polyphenols as Revealed by Spectroscopic Techniques: Implications in the Identification and Characterization of Iron Gall Inks in Historical Manuscripts. *ACS Omega* **2022**, *7*, 27937–27949. [CrossRef]
37. Li, D.; Chen, X.; Liu, C.; Tian, J.; Li, F.; Liu, Y. Suppression of pyrite oxidation by co-depositing bio-inspired PropS-SH-tannic acid coatings for the source control acid mine drainage. *Sci. Total. Environ.* **2023**, *862*, 160857. [CrossRef]
38. Fan, H.; Wang, J.; Jin, Z. Tough, Swelling-Resistant, Self-Healing, and Adhesive Dual-Cross-Linked Hydrogels Based on Polymer–Tannic Acid Multiple Hydrogen Bonds. *Macromolecules* **2018**, *51*, 1696–1705. [CrossRef]
39. Sun, D.; Li, M.; Zhang, M.; Cui, R.; Yang, Z.; Yu, L.; Wang, D.; Yao, W. Utilization and Mechanisms of Tannic Acid as a Depressant for Chalcopyrite and Pyrite Separation. *ACS Omega* **2023**, *8*, 30474–30482. [CrossRef]
40. You, G.-X.; Yu, C.-C.; Lu, Y.; Dang, Z. Evaluation of the protective effect of polysiloxane coating on pyrite with electrochemical techniques. *Electrochim. Acta* **2013**, *93*, 65–71. [CrossRef]
41. Cai, Y.; Pan, Y.; Xue, J.; Sun, Q.; Su, G.; Li, X. Comparative XPS study between experimentally and naturally weathered pyrites. *Appl. Surf. Sci.* **2009**, *255*, 8750–8760. [CrossRef]
42. Feng, X.; Chen, Z.; Wang, S.; Cen, L.; Ni, B.J.; Liu, Q. Insights into the weathering behavior of pyrite in alkaline soil through electrochemical characterizations: Actual hazards or potentially benefits? *J. Hazard. Mater.* **2023**, *451*, 131145. [CrossRef]
43. Solmaz, R.; Karda, G.; Yazc, B.; Erbil, M. Adsorption and corrosion inhibitive properties of 2-amino-5-mercapto-1,3,4-thiadiazole on mild steel in hydrochloric acid media. *Colloids Surf. A* **2008**, *312*, 7–17. [CrossRef]
44. Zheng, K.; Li, H.; Xu, L.; Li, S.; Wang, L.; Wen, X.; Liu, Q. The influence of humic acids on the weathering of pyrite: Electrochemical mechanism and environmental implications. *Environ. Pollut.* **2019**, *251*, 738–745. [CrossRef]
45. Mukarrom, F.; Pranoto; Karsidi, R.; Gravitiani, E.; Astuti, F.; Maharditya, W. The assessment of claystone, quartz and coconut shell charcoal for adsorbing heavy metals ions in acid mine drainage. *IOP Conf. Ser. Mater. Sci. Eng.* **2020**, *858*, 012040. [CrossRef]
46. Shafiq, M.; Yasin, T.; Saeed, S. Synthesis and characterization of linear low-density polyethylene/sepiolite nanocomposites. *J. Appl. Polym. Sci.* **2011**, *123*, 1718–1723. [CrossRef]
47. Justin Dhanaraj, C.; Sivasankaran Nair, M. Synthesis, characterization, and antimicrobial studies of some Schiff-base metal (II) complexes. *J. Coord. Chem.* **2009**, *62*, 4018–4028. [CrossRef]
48. Kaghazchi, L.; Naderi, R.; Ramezanzadeh, B. Synergistic mild steel corrosion mitigation in sodium chloride-containing solution utilizing various mixtures of phytic acid molecules and Zn2+ ions. *J. Mol. Liq.* **2021**, *323*, 114589. [CrossRef]
49. Berkh, K.; Rammlmair, D. The effect of Co substitution on the Raman spectra of pyrite: Potential as an assaying tool. *Eur. J. Mineral.* **2022**, *34*, 259–274. [CrossRef]
50. Chan-Rosado, G.; Pech-Canul, M.A. Influence of native oxide film age on the passivation of carbon steel in neutral aqueous solutions with a dicarboxylic acid. *Corros. Sci.* **2019**, *153*, 19–31. [CrossRef]
51. Mei, L.; Liao, L.; Wang, Z.; Xu, C. Interactions between Phosphoric/Tannic Acid and Different Forms of FeOOH. *Adv. Mater. Sci. Eng.* **2015**, *2015*, 1–10. [CrossRef]
52. Wang, B.; Moon, J.R.; Ryu, S.; Park, K.D.; Kim, J. Antibacterial 3D graphene composite gel with polyaspartamide and tannic acid containing in situ generated Ag nanoparticle. *Polym. Compos.* **2020**, *41*, 2578–2587. [CrossRef]
53. Geißler, S.; Barrantes, A.; Tengvall, P.; Messersmith, P.B.; Tiainen, H.J.L. Deposition kinetics of bioinspired phenolic coatings on titanium surfaces. *Langmuir* **2016**, *32*, 8050–8060. [CrossRef] [PubMed]
54. Primo, E.N.; Bracamonte, M.V.; Luque, G.L.; Bercoff, P.G.; Leiva, E.P.M.; Barraco, D.E. Mechanochemically synthesized pyrite and its electrochemical behavior as cathode for lithium batteries. *J. Solid State Electrochem.* **2019**, *23*, 1929–1938. [CrossRef]
55. Zhu, J.; Xian, H.; Lin, X.; Tang, H.; Du, R.; Yang, Y.; Zhu, R.; Liang, X.; Wei, J.; Teng, H.H.; et al. Surface structure-dependent pyrite oxidation in relatively dry and moist air: Implications for the reaction mechanism and sulfur evolution. *Geochim. Cosmochim. Acta* **2018**, *228*, 259–274. [CrossRef]
56. Herbert, F.W.; Krishnamoorthy, A.; Ma, W.; Van Vliet, K.J.; Yildiz, B. Dynamics of point defect formation, clustering and pit initiation on the pyrite surface. *Electrochim. Acta* **2014**, *127*, 416–426. [CrossRef]